PHYSICAL REVIEW MATERIALS **6**, 036201 (2022)

**Editors' Suggestion**

# Quasiparticle energies and optical excitations of 3C-SiC divacancy from *GW* and *GW* plus Bethe-Salpeter equation calculations

Weiwei Gao,[1,2,*] Felipe H. da Jornada,[3,4,5,*] Mauro Del Ben,[6,*] Jack Deslippe,[7] Steven G. Louie,[4,5,†] and James R. Chelikowsky[1,8,9,‡]

[1] *Center for Computational Materials, Oden Institute for Computational Engineering and Sciences, The University of Texas at Austin, Austin, Texas 78712, USA*
[2] *Key Laboratory of Materials Modification by Laser, Ion and Electron Beams, Ministry of Education, Dalian University of Technology, Dalian 116024, China*
[3] *Department of Materials Science and Engineering, Stanford University, Stanford, California 94305, USA*
[4] *Department of Physics, University of California at Berkeley, California 94720, USA*
[5] *Materials Sciences Division, Lawrence Berkeley National Laboratory, Berkeley, California 94720, USA*
[6] *Computational Research Division, Lawrence Berkeley National Laboratory, Berkeley, California 94720, USA*
[7] *NERSC, Lawrence Berkeley National Laboratory, Berkeley, California 94720, USA*
[8] *Department of Physics, The University of Texas at Austin, Austin, Texas 78712, USA*
[9] *McKetta Department of Chemical Engineering, The University of Texas at Austin, Austin, Texas 78712, USA*

(Received 20 December 2021; accepted 16 February 2022; published 17 March 2022)

Excitons localized around point defects in semiconductors are promising candidates for long-lived and photon-addressable qubits. However, their microscopic origin is difficult to characterize due to the computational complexity of studying large systems with defects. Here we study the quasiparticle and optical absorption spectrum of the divacancy defect in 3C-SiC, a prototypical defect for quantum information applications, by means of large-scale *GW* and *GW* plus Bethe-Salpeter equation calculations. Despite the presence of localized unoccupied quasiparticle states in the gap, we find that the low-energy excitonic states are made primarily of transitions from occupied defect states to continuum conduction states from SiC, especially from the *X* point of the Brillouin zone. The mixed character of defect states and bulk states of these low-energy exciton states is in contrast with the $NV^-$ center in diamond and the divacancy in 4H-SiC, where the deep defect levels are well separated from bulk states. Our calculations provide a quantitative prediction of the defect quasiparticle energy levels and a physical understanding of the zero-phonon absorption. They highlight the important role of frontier conduction bands in the optical properties and formation of low-energy excitons in 3C-SiC divacancy.

DOI: 10.1103/PhysRevMaterials.6.036201

## I. INTRODUCTION

Optically accessible deep-level defects in solids have the potential to function as quantum bits for quantum computing or quantum sensing applications [1,2]. Among numerous point defects, the negatively charged nitrogen-vacancy ($NV^-$) center is one of the most studied systems, demonstrating many key properties, including long spin coherence time at room temperature and a robust spin-photon interface [3,4]. However, the high cost of processing diamond, integrating it with established semiconducting fabrication practices, and scaling up the number of coherently coupled $NV^-$ centers still poses huge challenges for practical applications [4]. Recently, research efforts are shifting to defects in alternative semiconductors, such as divacancies in SiC polymorphs [5–8], silicon-vacancy centers in diamond [9–12], and rare-earth ions in solids [13–15] and so on [16–18]. Among them, experiments show that divacancies of 3C-SiC and 4H-SiC fulfill a few key requirements, such as single-defect addressability and high-fidelity spin-to-photon interfaces, which are critical for physical implementation of qubits [6]. Notably, the divacancy in 3C-SiC possesses a record-long Hahn-echo spin coherence time of one millisecond [6]. In addition to these advantages, SiC is widely used in industry and can be fabricated in high quality with lower costs than diamond [19].

The ground-state properties, such as formation energies, hyperfine coupling tensors, and zero field splittings, of SiC divacancies have been thoroughly studied by experiment and faithfully explained by theoretical calculations based on density functional theory (DFT) [20–23]. On the other hand, accurate theoretical calculations of excited-states properties, including the quasiparticle energies of defect states and optical excitations, are important for a quantitative understanding of the interactions between the defects and photon. As for divacancies in common SiC polymorphs, the 4H phase is the most studied one by both experiments and calculations. Excited-states properties of 4H-SiC divacancies, such as zero-phonon emission lines and the single-particle energies of deep defect states, were calculated using hy-

*These authors contributed equally to this work.
†sglouie@berkeley.edu
‡jrc@utexas.edu

 ©2022 American Physical Society

brid functionals [18,20,22]. Furthermore, the energies of many-body excited states with different spin multiplicities of 4H-SiC divacancy were calculated with active-space configuration interaction calculations [24,25]. However, despite many recent experimental efforts on exploiting the optical properties of 3C-SiC divacancies for quantum photonic applications [26–28], accurate and thorough computational studies on the excited-states properties of 3C-SiC divacancy are still lacking, e.g., no conclusive computations for quasiparticle energies of defect states and the characters low-energy optical transitions exist.

In this context, DFT in principle can yield accurate ground state energy and density, but it cannot accurately yield excited-states properties. Recently, several methods designed specifically for excited-states properties, such as active-space configuration interaction and the *GW* approximation, have been applied to study defects [17,18,24,25,29–32]. Among them, *GW* approximation and *GW* plus Bethe-Salpeter equations (*GW*-BSE), which are based on well-established many-body perturbation theories, can give accurate descriptions for the single-particle energy levels and spin-conserving excitations [33,34]. Unfortunately, the cubic to quartic scaling and nontrivial convergence behavior of typical *GW* implementation [35–38], as well as the $N^6$ scaling of BSE, hinder wide applications of these methods to defect systems [39,40]. Moreover, in practical calculations, defects are typically modeled with a finite-size nanocluster or a periodic supercell. To minimize artifacts from periodic images, large supercells containing hundreds to thousands of atoms are required, posing further difficulties for *GW* and *GW*-BSE calculations. Due to these reasons, *GW* and *GW*-BSE calculations are not routinely carried out for defects in solids, while DFT calculations based on generalized-gradient approximation (GGA) or hybrid functionals, which have relatively low computational costs, are often used for the calculation of defect levels and zero phonon optical transition lines neglecting electron-hole transitions [3,16,18,20,22,41–44].

Here we study quasiparticle energies and spin-conserved optical absorption spectra of the divacancy defect in 3C-SiC with large-scale *GW* and *GW*-BSE calculations. In the study of the optical properties, we treat the system as two spin fluids and neglect all spin multiplet effects for both the ground and excited states. Our calculations explicitly evaluate the full frequency dependence of the dielectric matrix without resorting to plasmon-pole approximations [45]. Different from the 4H-SiC divacancy and diamond $NV^-$ center, our calculations reveal that unoccupied defect quasiparticle states in 3C-SiC are relatively shallow. Our *GW*-BSE calculations yield accurate zero-phonon line energy within the two-spin-fluid formalism and show the lowest-energy exciton states involve transitions between localized defect and bulk continuum states, while these low-energy excitons are still fairly localized near the divacancy.

## II. COMPUTATION DETAILS

We use the Perdew-Burke-Ernzerhof (PBE) exchange-correlation functional [46] for collinear spin density functional theory (DFT) calculations. The structures are optimized with the real-space DFT code PARSEC [47,48] using a real-space grid of 0.285 bohr spacing. The optimized lattice constant of bulk 3C-SiC is 4.379 Å, agreeing well with the experimental value [49]. The divacancy is modelled with a supercell. Here we keep the lattice constant as that of bulk SiC and relax atomic coordinates until residue forces on each atom are less than $1 \times 10^{-4}$ Ryd/Bohr. By testing the convergence of the DFT results with respect to the supercell size, we find the energy separation between the conduction band minimum (CBM) and spin up state with the *e* symmetry converge within 50 meV with a 510-atom supercell and 2 meV with a 998-atom supercell, as shown in Fig. 1(a).

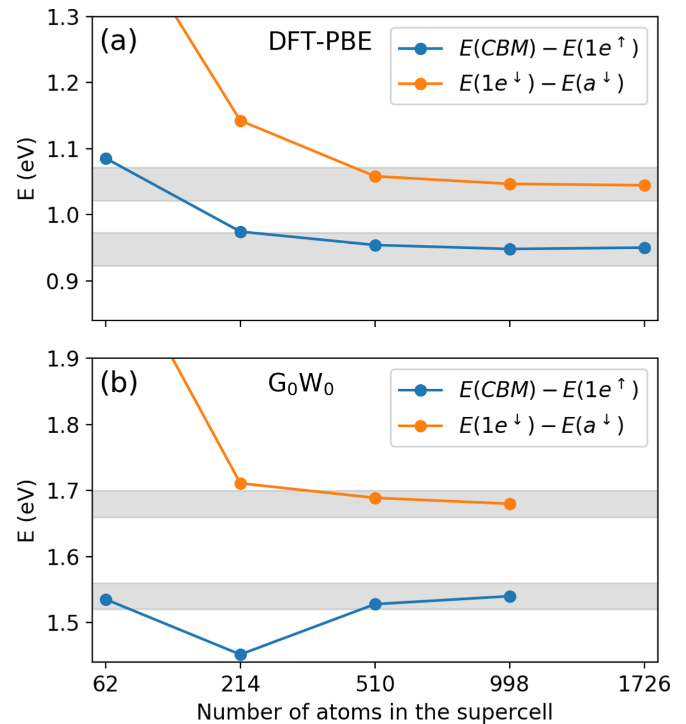


FIG. 1. Convergence of single-particle transition energies calculated using (a) DFT and (b) $G_0W_0$ with supercell sizes. The shadow areas highlight the energy ranges of 40 meV around the data calculated with the 998-atom supercell. The labels of defect states are explained in Sec. III.

*GW* and *GW*-BSE calculations are carried out with the BERKELEYGW package [33,34,50]. The starting points for *GW*-BSE calculations are the mean-field wave functions calculated with PBE functional [46] and SG15 Optimized Norm-Conserving Vanderbilt pseudopotentials [51–53] using QUANTUM ESPRESSO package [54,55]. The mean-field wavefunctions are calculated with an 50 Ryd cut-off and sampled at Γ point. We perform "one-shot" *GW* calculations ($G_0W_0$ approximation) at the full-frequency level within the contour deformation formalism [56,57]. We also tested the convergence of $G_0W_0$ calculations with respect to supercell sizes. Figure 1(b) shows that the $G_0W_0$ results calculated with 510-atom and 998-atom supercells only differ by up to 20 meV, which suggests a reasonably good convergence. In the following discussions, the *GW* calculation results for the divacancy are performed with a 998-atom supercell, unless otherwise mentioned. The frequency dependent parts of dielectric functions are obtained within the static-subspace

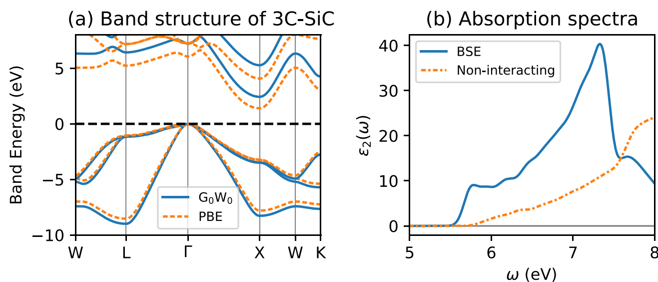


FIG. 2. (a) Quasiparticle band structure of pristine 3C-SiC computed within DFT using Perdew-Burke-Ernzerhof (PBE) functional and within the $G_0W_0$ approximation. (b) Comparison between the imaginary part of the dielectric function calculated with $GW$-BSE and with noninteracting particle approximation. A Gaussian smearing of 0.05 eV is used for calculating dielectric function.

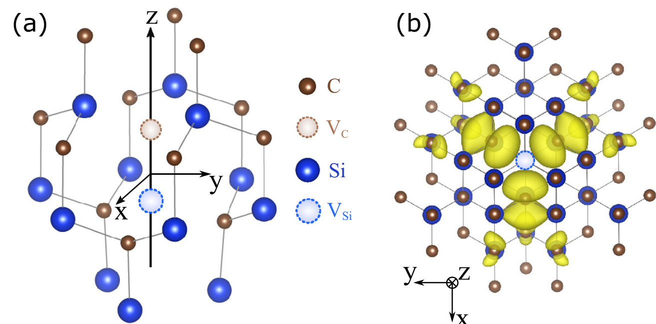


FIG. 3. (a) The structure of divacancy in 3C-SiC [64]. (b) Top view of a divacancy. The isosurface of the net spin charge density $|\rho_\uparrow(\mathbf{r}) - \rho_\downarrow(\mathbf{r})|$ is shown in yellow.

approximation [45,58–60]. The static-subspace approximation method is a low-rank approximation method for calculating the frequency-dependent dielectric matrix. In brief, we first calculate the eigenvalues and eigenvectors of the static dielectric matrix. Then we pick the eigenvectors with large eigenvalues as the basis set functions to represent dielectric matrices of finite frequencies. This method has been discussed in detail in Ref. [45]. To converge the $G_0W_0$ calculation with a 998-atom supercell, we employed up to $18 \times 10^3$ eigenvectors for the static-subspace basis expansion. For frequency integration, we used 16 imaginary frequencies and 34 frequencies on the real axis up to a maximum of 8 eV. With the sum-over-bands $GW$ implementation used in our work, the equations of irreducible polarizability and self-energy include a summation over all empty states. To reduce the cost for summing over many empty states, we employ the stochastic pseudobands method. With this method, one combines several high-energy orbitals into a single unnormalized states to represent high-energy empty states [45,61]. The stochastic pseudobands allow us to effectively include the whole Hilbert space for the evaluation of the polarizability and self energy. A similar idea was also reported in Ref. [62]. For the $GW$-BSE calculation of a 998-atoms supercell, we consider the Γ point and the transitions between 40 conduction bands and 40 valence bands for each spin channel. Our tests show that these numbers of bands can converge the absorption spectrum up to $\omega = 2.6$ eV. For pristine bulk 3C-SiC, we considered three conduction bands, three valence bands, and a $24 \times 24 \times 24$ $q$-points grid for optical absorption spectrum calculations.

## III. RESULTS AND DISCUSSION

Before studying the divacancy, we briefly discuss the electronic structure of bulk 3C-SiC. As shown in Fig. 2(a), pristine 3C-SiC has an indirect band gap between valence band maximum (VBM) at Γ and CBM at $X$. There are three equivalent $X$ points on the edge of the Brillouin zone (BZ), so the CBM is triply degenerate. Our DFT-PBE calculation predicts an indirect band gap of 1.4 eV. With the $GW$ approximation at the $G_0W_0$ level, the quasiparticle self-energy effect opens up the band gap to 2.3 eV, which agrees well with the experimental value of 2.36 eV [63]. In Fig. 2(b), we compare the optical absorption spectrum of 3C-SiC calculated with $GW$-BSE and a noninteracting particle approximation. Within the noninteracting particle approximation, the lowest single-particle transition, which corresponds to the direct transition at $X$, has an $GW$ energy of 5.64 eV. In comparison, the energy of the lowest optically active exciton calculated with $GW$-BSE is 5.45 eV, which corresponds to an exciton binding energy of 0.19 eV.

In Fig. 3, we show the structure of a divacancy $V_C V_{Si}$ in 3C-SiC, where the carbon vacancy $V_C$ and silicon vacancy $V_{Si}$ are placed along the $z$ axis [$z$ axis is along the (111) direction]. Similarly to the diamond $NV^-$ center, a divacancy in 3C-SiC has the $C_{3v}$ point group symmetry, and the divacancy in 3C-SiC induces sizable distortions to the positions of nearby atoms. In particular, the nearest neighboring carbon atoms shift away from the silicon vacancy $V_{Si}$, making the distance $d_{C\text{-}C}$ between nearest carbon atoms 3.298 Å, larger than the bulk value of 3.096 Å. The positions of the nearest neighboring silicon atoms show smaller distortions than carbon atoms. The relaxed distance $d_{Si\text{-}Si}$ between nearest neighboring Si is 3.092 Å, close to the bulk value. DFT calculations within GGA using PBE functional show a spin-polarized ground state with a magnetic moment of $2\mu_B$ per each divacancy. We show the isosurface of the net spin charge density $|\rho_\uparrow(\mathbf{r}) - \rho_\downarrow(\mathbf{r})|$ in Fig. 3(b), which also demonstrates the $C_{3v}$ symmetry of the system. The spin density is mostly localized at the neighboring carbon atoms and has the symmetry of $p$ orbitals.

Next, we investigate the electronic structure of 3C-SiC divacancy in terms of the single-quasiparticle energy levels. A divacancy $V_{Si}V_C$ in 3C-SiC creates six dangling bonds, which form six defect states per each spin channel within this limited Hilbert space. These localized defect states are classified into either the nondegenerate $a_1$ states or doubly-degenerate $e$ states according to their symmetry properties. To identify all the localized states from our calculation, we evaluate the inverse participation ratio (IPR), defined as IPR $= \int |\phi(\mathbf{r})|^4 d^3r$, for states $\phi(\mathbf{r})$; a larger IPR is an indication that $\phi$ is more localized in real space. As shown in Fig. 4(a), we plot the IPRs of states close to the band gap from a DFT-PBE calculation using a supercell of 998 atoms and a Γ-point sampling. The states inside the shaded region have IPRs ranging from $\sim 10^{-5}$ to $8 \times 10^{-5}$ and are recognized as localized defect states. We identify one $a_1$ state and two pairs of $e$ states, which are labeled as $1e^\sigma = \{1e_x^\sigma, 1e_y^\sigma\}$ and $2e^\sigma = \{2e_x^\sigma, 2e_y^\sigma\}$ according to their energy ordering, for two spin channels $\sigma = \downarrow, \uparrow$. Two

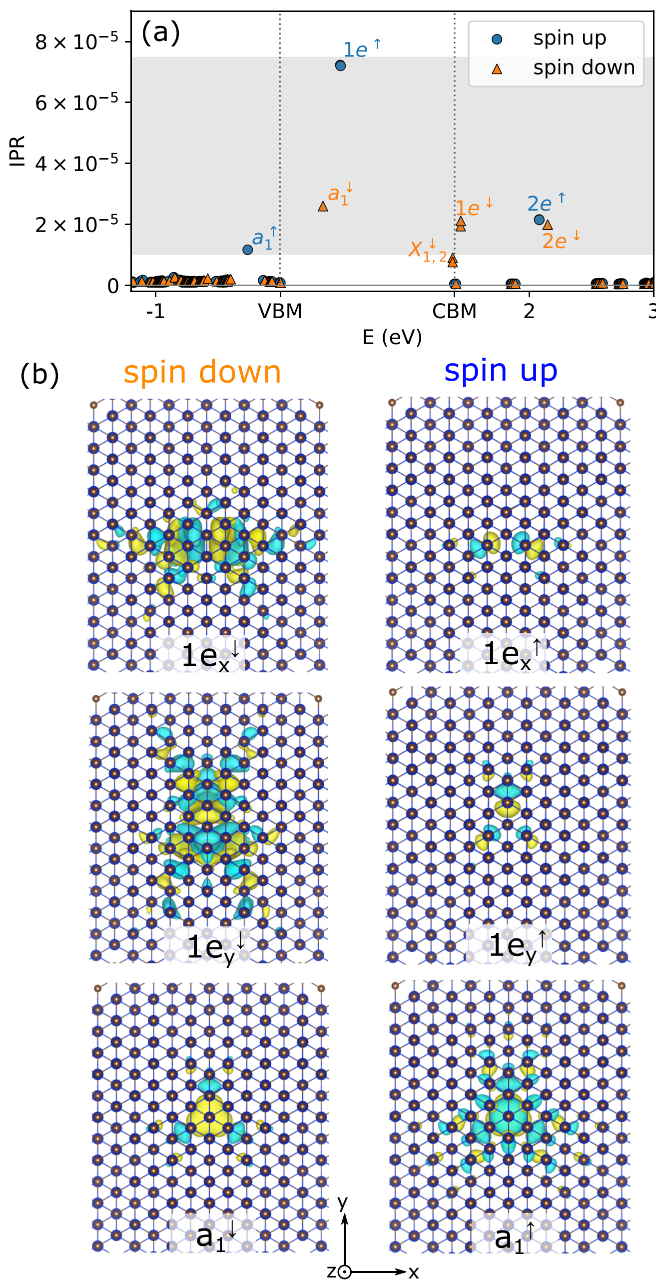


FIG. 4. (a) The inverse participation ratio for states close to the Fermi energy. (b) The isosurface of $\mathrm{sgn}(\phi(\mathbf{r}))|\phi(\mathbf{r})|^2$ of $a_1^{\sigma}$ and $1e^{\sigma} = \{1e_x^{\sigma}, 1e_y^{\sigma}\}$ states for two spin channels. Each isosurface includes 50% of the charge density contributed by the corresponding orbital.

more $a_1$ states are located out of the plotting range and mixed with valence bands. Conforming with previous group-theory analysis [65], our results show that $e$ states have higher energies than the $a_1$ state. Among all localized defect states identified, the spin-down $a_1^{\downarrow}$ state and the spin-up $1e^{\uparrow}$ states are located deep inside the band gap, while the others are located either below the VBM or above the CBM as resonances.

In addition to these localized defect states, we also find a pair of spin-down states, denoted as $X_1^{\downarrow}$ and $X_2^{\downarrow}$, displays large IPRs that are one order of magnitude larger than typical extended bulk states, as shown in Fig. 4(a). $X_1^{\downarrow}$ and $X_2^{\downarrow}$ are close to CBM and show strong hybridization between spin-down $1e^{\downarrow}$ and conduction bands. We plot the isosurface of the charge density of selected defect states in Fig. 4(b). One can clearly see that the hybridization makes the $1e^{\downarrow}$ states more delocalized in real space than $a_1^{\downarrow}$ and $1e^{\uparrow}$, which are inside the band gap and have minor hybridization with bulk states.

We obtain a deeper understanding on the nature of states $X_1^{\downarrow}$ and $X_2^{\downarrow}$ by computing the matrix elements $\langle\phi_1|R|\phi_2\rangle = \int_{\Omega_{\mathrm{cell}}}\phi_1^*(\mathbf{r})R\phi_2(\mathbf{r})d^3r$, where $R = |\mathbf{r}|$ is the distance to the center of a divacancy and $\Omega_{\mathrm{cell}}$ is the real-space domain of a supercell. We find the expectation value $\langle\phi|R|\phi\rangle$ is an intuitive measure to distinguish localized and extended states. Related measures were also used [66,67] in the literature. A larger expectation value $\langle\phi|R|\phi\rangle$ suggests that $\phi(\mathbf{r})$ is more extended in real space. We find $\langle X_1^{\downarrow}|R|X_1^{\downarrow}\rangle = \langle X_2^{\downarrow}|R|X_2^{\downarrow}\rangle \approx$ 14 Bohr, which is quite close to $\langle 1e^{\downarrow}|R|1e^{\downarrow}\rangle \approx 12$ Bohr. For comparison, the expectation value of $R$ for typical bulk states ranges from 18 to 22 Bohr, which is dictated by the size of the supercell used. When we then diagonalize the matrix $\langle\phi_1|R|\phi_2\rangle$ including four states that are nearly degenerate within our DFT calculations (i.e., the manifold of $X_{1,2}^{\downarrow}$ and the two spin-down $1e^{\downarrow}$ states), we find two pairs of doubly degenerate eigenstates. One pair of degenerate eigenstates has a small expectation value of $\langle R\rangle = 6.5$ Bohr and, apart from the stronger localization, is very similar to the two $1e^{\downarrow}$ states. The remaining degenerate eigenstates have a large expectation value of $\langle R\rangle = 19.6$ Bohr and their wave functions resemble that of the CBM at the $X$ point of bulk SiC. This strongly suggests that the two $X_{1,2}^{\downarrow}$ and two $1e^{\downarrow}$ states are hybrid states made mostly out of extended CBM states and localized defect orbitals, respectively. These states are parts of the defect resonance from two otherwise localized states if they were in the gap, and there would be more $X$-like states (in the same energy range) as the number of $k$ points increases in the sampling in the supercell calculation.

In Figs. 5(a)–5(c), we compare the energy levels near the band edge of 4H-SiC divacancy, diamond $\mathrm{NV}^-$ center, and 3C-SiC divacancy, calculated within DFT with the PBE functional. Clearly, the defect states associated with low-energy and optically active transitions, such as the $a_1^{\downarrow}$ and $e^{\downarrow}$ of 4H-SiC divacancy and diamond $\mathrm{NV}^-$ center, are separated from the bulk states, and the lowest-energy single-particle transition is $(a_1^{\downarrow} \rightarrow 1e^{\downarrow})$. In contrast to 4H-SiC and diamond, 3C-SiC has a much smaller band gap, so it is not surprising to see hybridization between certain localized defect states and bulk states, as discussed before. As shown in Fig. 5(c), the DFT-PBE states $1e^{\downarrow}$ are above the CBM, and the lowest-energy band-to-band transition of the 3C-SiC divacancy is $(1e_1^{\uparrow} \rightarrow \mathrm{CBM}^{\uparrow})$. Compared to DFT-PBE results, the $G_0W_0$ approximation increases the separations between deep defect states and bulk states. In particular, states in the middle of band gap, namely $a_1^{\downarrow}$ and $1e^{\uparrow}$, are further separated from the VBM. Notably, $G_0W_0$ self-energy effects push $1e^{\downarrow}$ lower than the conduction bands.

We compute the imaginary part of the dielectric function $\epsilon_2(\omega)$ using the independent-particle approximation (with the $G_0W_0$ state energies) and $GW$-BSE approach, as shown in Figs. 6(a) and 6(b). Full relativistic effects and spin-flipping optical transitions are not considered in our calculations. To

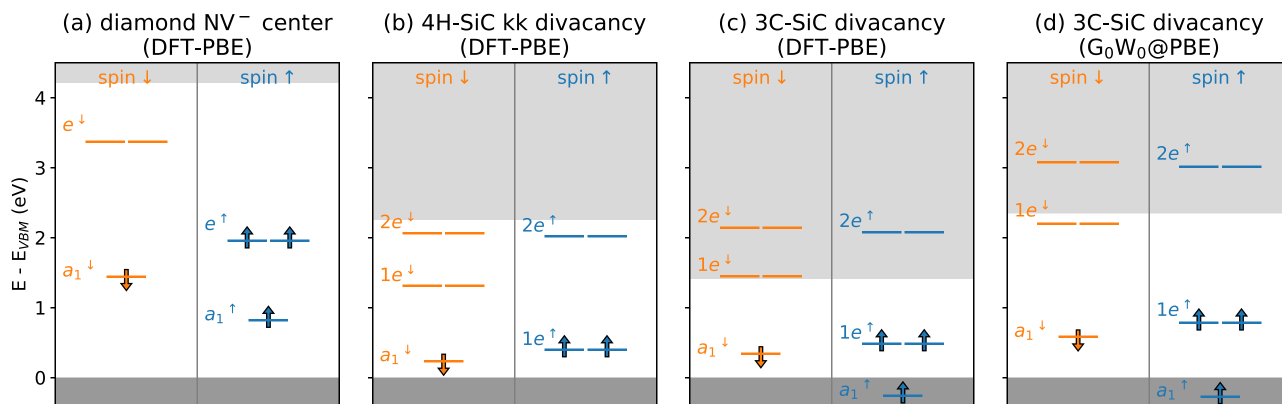


FIG. 5. Single particle energy levels of (a) diamond NV$^-$ (b) 4H-SiC *kk* divacancy. (There are two different lattice sites, namely, the hexagonal and cubic sites in 4H-SiC. The ‘‘*kk* divacancy” means both $V_{\rm Si}$ and $V_{\rm C}$ are located at cubic sites.) (c) 3C-SiC divacancy calculated with a DFT-PBE approach. (d) Defect energy levels of 3C-SiC divacancy calculated with $G_0W_0$ approximation. Horizontal lines represent localized defect states, and gray shaded areas are extended bulk states.

analyze the characters of low-energy optical excitations of the 3C-SiC divacancy within our formalism, we classify optical transitions according to the characters of the electron and hole states involved in a transition, as shown in Fig. 6(c). We define a subspace $D$ of defect states: $D = \{a_1^\sigma, X_1^\downarrow, X_2^\downarrow, 1e^\sigma, 2e^\sigma\}$, where $\sigma = \uparrow, \downarrow$ and all the other states are recognized as bulk states. Under the noninteracting particle approximation (using $G_0W_0$ energies), the lowest-energy excitation corresponds to the transition from $1e^\uparrow$ to the CBM$^\uparrow$ with the energy of 1.55 eV. The lowest-energy defect-to-defect transitions ($a_1^\downarrow \rightarrow 1e^\downarrow$) and ($a_1^\downarrow \rightarrow X_{1,2}^\downarrow$) are located at 1.67 eV and at 1.74 eV, respectively. Next, we perform first-principles *GW*-BSE calculations and find that excitonic effects lower the absorption edge to 1.06 eV, giving a large exciton binding energy of 0.49 eV. Interestingly, the calculated $\epsilon_2(\omega)$ in the low-energy range becomes smaller with the inclusion of excitonic effects. This observation is in stark contrast to common bulk or 2D materials, where excitonic effects usually enhance the low-energy absorption peaks. The reason behind this contrasting behavior is due to the different nature of the low-energy exci-

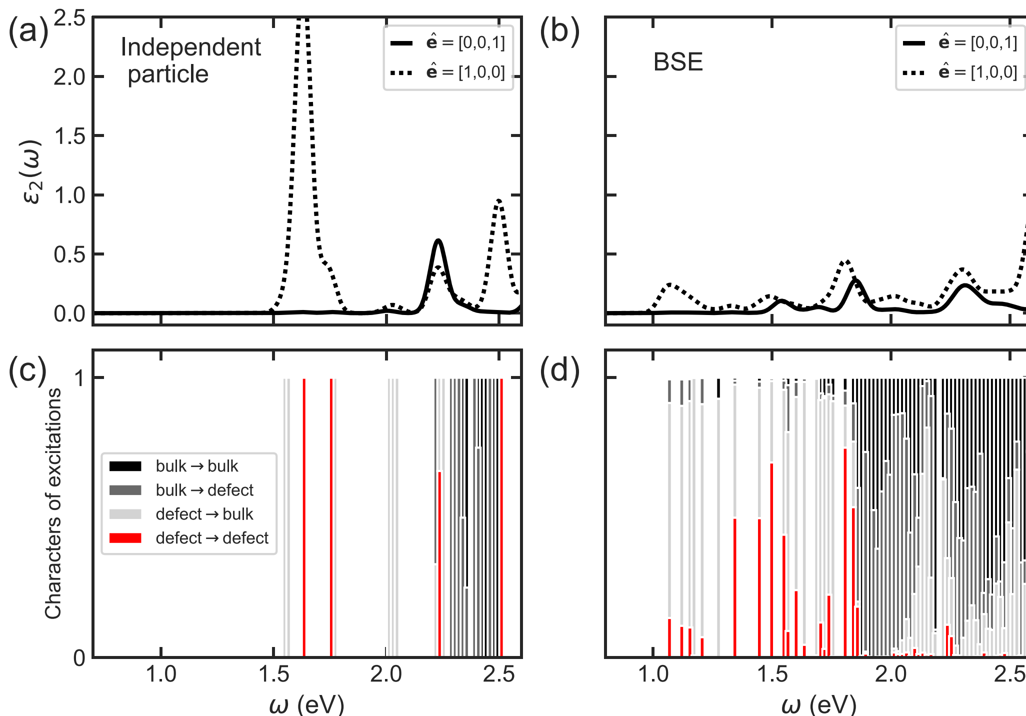


FIG. 6. Imaginary part of frequency-dependent dielectric functions (absorption spectra) of a 3C-SiC divacancy calculated with (a) independent particle approximation with the $G_0W_0$ energies and (b) *GW*-BSE approach. The defect is modelled with a 998-atom supercell, and a Gaussian smearing of 0.035 eV is used for the calculation of dielectric function. Characters of optical excitations calculated with (c) independent particle approximation with the $G_0W_0$ energies and (d) *GW*-BSE approach. Note that a vertical line in (c) and (d) may correspond to several optical excitations.

tonic states compared to independent-particle transitions. As we discussed later, low-energy excitons have significant contributions from transitions to bulk states of different momenta, as finite-momenta transitions can mix with zero-momentum transitions since translational symmetry in SiC is broken due to the presence of a defect.

We also find the low-energy absorption spectra strongly depend on the polarization direction $\mathbf{e}$ of the incident light. As shown in Fig. 6(a), the single-particle transitions ($a_1^\downarrow \rightarrow 1e^\downarrow$) and ($a_1^\downarrow \rightarrow X_{1,2}^\downarrow$) show strong absorption of transversely polarized light ($\mathbf{e} = [1, 0, 0]$) but become dark for longitudinally polarized light ($\mathbf{e} = [0, 0, 1]$). The linear dichroism can be qualitatively explained by dipole selection rules. Within the independent-particle approximation, the optical transition matrix element of a transition between a valence state $v$ and a conduction state $c$ is proportional to $|\mathbf{e} \cdot \langle v|\hat{\mathbf{v}}|c\rangle|^2$, where $\hat{\mathbf{v}} = \hat{\mathbf{v}}_x + \hat{\mathbf{v}}_y + \hat{\mathbf{v}}_z$ is the velocity operator. Since $[\hat{\mathbf{v}}_x, \hat{\mathbf{v}}_x]$, $[X_1^\downarrow, X_2^\downarrow]$, and $1e^\downarrow = [1e_x^\downarrow, 1e_y^\downarrow]$ transform according to the $e$ representation and $a_1^\downarrow$ is fully symmetric under the $C_{3v}$ group, the matrix elements $\langle 1e_x|\hat{\mathbf{v}}_x|a_1\rangle$ and $\langle 1e_y|\hat{\mathbf{v}}_y|a_1\rangle$ are generally nonzero, while $\langle 1e_x|\hat{\mathbf{v}}_z|a_1\rangle$ and $\langle 1e_y|\hat{\mathbf{v}}_z|a_1\rangle$ vanish according to the dipole-selection rules. Consequently, ($a_1^\downarrow \rightarrow 1e^\downarrow$) and ($a_1^\downarrow \rightarrow X_{1,2}^\downarrow$) transitions are bright under transversely polarized light as we observed in independent-particle-approximation calculations. Similarly, when we solve the BSE, we observe that the lowest-energy excitons between 1.0 and 1.3 eV are bright under longitudinal polarization but dark under transverse polarization. The optical oscillator strength is contributed to mainly by transitions between defect states.

We analyze our results including electron-hole interactions by writing each excitonic state $|S\rangle$, within the Tamm-Dancoff approximation, as a linear combination of electron-hole pairs

$$|S\rangle = \sum_v^{\text{hole}} \sum_c^{\text{elec}} A_{vc}^S |v\rangle|c\rangle,$$

where $v$, $c$, and $S$ are the index for occupied, unoccupied, and excitonic states, respectively, and $A_{vc}^S$ are the eigenvectors of the BSE and satisfy the normalization relation $\sum_{vc} |A_{vc}^S|^2 = 1$.

The decomposition of excitonic states into different characters is shown in Fig. 6(d), where the length of each colored vertical line at energy $\omega$ is the weight of the corresponding type of single-particle transition of the excitons within an energy range $[\omega - \delta/2, \omega + \delta/2]$, where $\delta = 0.02$ eV. For example, the length of red lines is the weight of defect-to-defect transitions, defined as

$$w_{\text{defect}\rightarrow\text{defect}}(\omega) = \frac{\int_{\omega-\delta/2}^{\omega+\delta/2} \sum_S \sum_{v,c\in D} \delta(E - \Omega_S)|A_{vc}^S|^2 dE}{\int_{\omega-\delta/2}^{\omega+\delta/2} \sum_S \delta(E - \Omega_S) dE},$$

where defect states $D$ are defined before and $\Omega_S$ are the energy of excitonic states $|S\rangle$. For low-energy excitons below 1.3 eV, the dominant characters are defect-to-bulk transitions, such as ($1e^\uparrow \rightarrow \text{CBM}^\uparrow$), mixed with a small amount of defect-to-defect transitions. Some of the excitons between 1.3 to 1.8 eV have large components of defect-to-defect transitions. For excitons with energies ranging from 1.8 to 2.6 eV, transitions involving bulk states are dominant. We note that the bulk-to-bulk transitions contributing to low-energy excitons (less than 2.6 eV) originate from indirect transitions between a valence electron at $\Gamma$ and an unoccupied state at the $X$ point of the BZ in pristine 3C-SiC. These bulk-to-bulk transitions have negligible contributions to the optical transition matrix elements.

TABLE I. Excitons with large contributions from single-particle transitions from $a_1^\downarrow$ to $\{X_1^\downarrow, X_2^\downarrow, 1e^\downarrow\}$.

| Exciton energy $\Omega_S$ (eV) | $\lvert A_{vc}^S\rvert^2$ $c = X_1^\downarrow$, $v = a_1^\downarrow$ | $c = X_2^\downarrow$, $v = a_1^\downarrow$ | $c = 1e_x^\downarrow$, $v = a_1^\downarrow$ | $c = 1e_y^\downarrow$, $v = a_1^\downarrow$ |
|---|---|---|---|---|
| 1.06 | 0.02 | 0.02 | 0.03 | 0.07 |
| 1.11 | 0.07 | 0.00 | 0.04 | 0.00 |
| 1.14 | 0.00 | 0.08 | 0.00 | 0.02 |
| 1.33 | 0.13 | 0.19 | 0.04 | 0.08 |
| 1.43 | 0.21 | 0.03 | 0.16 | 0.00 |
| 1.49 | 0.03 | 0.15 | 0.06 | 0.15 |
| 1.59 | 0.02 | 0.05 | 0.06 | 0.06 |
| 1.80 | 0.09 | 0.04 | 0.12 | 0.04 |
| 1.84 | 0.02 | 0.08 | 0.03 | 0.12 |

The zero-phonon line of 3C-SiC divacancy corresponds to the excitation from ground state $^3A_2$ to the first spin-triplet excited state $^3E$ [6]. Within the single-particle terminology, this excitation corresponds roughly to promoting an electron from $a_1^\downarrow$ to $1e^\downarrow$. In Table I, we compare the components of the $a_1^\downarrow \rightarrow \{X_{1,2}^\downarrow, 1e^\downarrow\}$ transitions in selected excitons. The excitons at 1.33, 1.43, 1.49 eV have large contributions from ($a_1^\downarrow \rightarrow 1e^\downarrow$) and ($a_1^\downarrow \rightarrow X_{1,2}^\downarrow$) transitions. Our analysis also shows that, while the lowest-energy exciton at 1.06 eV only has a small fraction of $a_1^\downarrow \rightarrow \{X_{1,2}^\downarrow, 1e^\downarrow\}$ transitions, its oscillator strength mainly originates from these defect-to-defect transitions. The electron-hole interactions tend to reduce the defect-to-defect character of the lowest-energy exciton. Such a reduction of the defect-to-defect characters makes an exciton optically weaker compared to low-energy defect-to-defect transitions computed within the independent-particle picture.

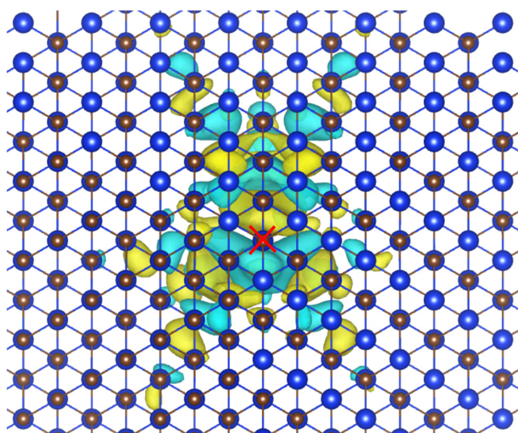

FIG. 7. The lowest-energy exciton wave function $\Psi_S(\mathbf{r}_e, \mathbf{r}_h)$, where $\mathbf{r}_e$ and $\mathbf{r}_h$ are the electron and hole coordinates, respectively. $\mathbf{r}_h$ is fixed at the center of a divacancy, shown as a red cross here.

TABLE II. Comparisons between calculated excitation properties and experiment.

| Properties (eV) | cDFT $a_1^{\downarrow} \rightarrow X_{1,2}^{\downarrow}$ | cDFT $\vert 0\rangle \rightarrow \vert S_0\rangle$ | *GW*-BSE | Expt. [6] |
|---|---|---|---|---|
| Anti-Stokes shift | 0.095 | 0.09 | | |
| Stokes shift | 0.11 | 0.05 | | |
| Vertical excitation | 1.06 | 1.17 | 1.06 | |
| Zero-phonon line | 0.95 | 1.12 | 1.01 | 1.12 |

We plot the wave function $\Psi_S(\mathbf{r}_e, \mathbf{r}_h)$ of the lowest-energy exciton in Fig. 7, with the hole position $\mathbf{r}_h$ kept at the center of a divacancy. Despite the significant contributions from conduction states with extended features, the exciton wave function is still highly localized near the divacancy, showing the symmetry of $1e^{\downarrow}$ states.

We compare the vertical transition energy and zero-phonon line of the 3C-SiC divacancy estimated with constrained DFT (cDFT) and first-principles *GW*-BSE approaches, as shown in Table II. We performed cDFT calculations in two different excited-states configurations. The first cDFT calculation depopulates $a_1^{\downarrow}$ and populates one of the $X_{1,2}^{\downarrow}$ states. In this calculation, our result underestimates the zero-phonon line by around 0.17 eV. Incidentally, the first cDFT and *GW*-BSE calculations yield the same vertical excitation energy. For the second cDFT calculation, we set the excited-states configuration according to the lowest exciton $|S_0\rangle$ of 1.06 eV, such that the occupation of an originally occupied state $|v\rangle$ is changed to $1.0 - \sum_c |A_{vc}^{S_0}|^2$, while that of an unoccupied state $|c\rangle$ is set to $\sum_v |A_{vc}^{S_0}|^2$. In the second cDFT calculation, we find a zero-phonon line of 1.12 eV, which agrees well with the experimental data [6]. We also find a smaller Stokes shift energy of 0.05 eV, which is smaller than the first cDFT calculation. Such a smaller Stokes shift is due to the large contribution from conduction bands to the exciton wave function. Since the conduction bands are more delocalized in real space, they tend to induce smaller atomic distortions to atoms near a divacancy than localized defect states and therefore a smaller Stokes shift. Combining the Stokes shift energy of 0.05 eV from the second cDFT calculation and exciton energy 1.06 eV, we get an ZPL energy 1.01 eV, which slightly underestimates the experimental value by 0.11 eV.

Finally, we note that, while current many-body perturbation theory approaches cannot be rigorously performed on degenerate ground states, as is the case with an open-shell system, spin-preserving neutral excitations energies are typically well described in such systems as diamond $NV^-$ center by *GW*-BSE calculations [68]. However, in order to accurately capture neutral excitations that involve a change in the total spin, one needs to resort to alternative techniques, such as full configuration-interaction calculations based on model systems or parameterized extended Hubbard models [29], that may provide a more faithful description.

## IV. CONCLUSIONS

We performed large-scale $G_0W_0$ and *GW* plus Bethe-Salpeter equation calculations for 3C-SiC divacancy, an emerging candidate for physical implementation of solid-states qubit. In contrast to the diamond $NV^-$ center and the 4H-SiC divacancy, where the deep defect levels are well separated from bulk states, our *GW* calculations show the optically active spin-down $e$ states are only 0.1 eV below the extended bulk states. Such a small separation leads to the emergence of excitons composed of transitions between defect-to-defect ($a_1^{\downarrow} \rightarrow 1e^{\downarrow}$), defect-to-bulk, and bulk-to-bulk transitions. Our independent-particle approximation and *GW*-BSE calculations show that the calculated absorption spectra display strong linear dichroism near the absorption edge, which is explained with dipole selection rules. Through *GW*-BSE calculations, we show that the lowest exciton has a large binding energy of 0.49 eV and observe that electron-hole interactions decrease the optical weight of the lowest-energy exciton. Substantial contribution from bulk states is observed in low-energy excitons, indicating the importance of bulk states in the understanding of the optical properties of 3C-SiC divacancy. Finally, we estimate the zero-phonon line using cDFT and *GW*-BSE methods and obtain good agreement with the experimental value.

## ACKNOWLEDGMENTS

We acknowledge support from the Center for Computational Study of Excited-State Phenomena in Energy Materials at the Lawrence Berkeley National Laboratory, which is funded by the U.S. Department of Energy, Office of Science, Basic Energy Sciences, Materials Sciences and Engineering Division under Contract No. DEAC02-05CH11231, as part of the Computational Materials Sciences Program. W.G. acknowledges support from Grant No. DUT21RC(3)033 funded by Fundamental Research Funds for the Central Universities and Grant No. 12104080 funded by National Science Foundation of China. Computational resources are provided by the National Energy Research Scientific Computing Center (NERSC) and the Texas Advanced Computing Center (TACC).

[1] J. R. Weber, W. F. Koehl, J. B. Varley, A. Janotti, B. B. Buckley, C. G. Van de Walle, and D. D. Awschalom, Proc. Natl. Acad. Sci. **107**, 8513 (2010).

[2] D. D. Awschalom, R. Hanson, J. Wrachtrup, and B. B. Zhou, Nat. Photonics **12**, 516 (2018).

[3] M. W. Doherty, N. B. Manson, P. Delaney, F. Jelezko, J. Wrachtrup, and L. C. Hollenberg, Phys. Rep. **528**, 1 (2013).

[4] A. Gali, Nanophotonics **8**, 1907 (2019).

[5] A. L. Falk, B. B. Buckley, G. Calusine, W. F. Koehl, V. V. Dobrovitski, A. Politi, C. A. Zorman, P. X.-L. Feng, and D. D. Awschalom, Nat. Commun. **4**, 1819 (2013).

[6] D. J. Christle, P. V. Klimov, C. F. de las Casas, K. Szász, V. Ivády, V. Jokubavicius, J. Ul Hassan, M. Syväjärvi, W. F. Koehl, T. Ohshima, N. T. Son, E. Janzén, A. Gali, and D. D. Awschalom, Phys. Rev. X **7**, 021046 (2017).

[7] N. T. Son, C. P. Anderson, A. Bourassa, K. C. Miao, C. Babin, M. Widmann, M. Niethammer, J. Ul Hassan, N. Morioka, I. G. Ivanov, F. Kaiser, J. Wrachtrup, and D. D. Awschalom, Appl. Phys. Lett. **116**, 190501 (2020).

[8] K. C. Miao, J. P. Blanton, C. P. Anderson, A. Bourassa, A. L. Crook, G. Wolfowicz, H. Abe, T. Ohshima, and D. D. Awschalom, Science **369**, 1493 (2020).

[9] C. Hepp, T. Müller, V. Waselowski, J. N. Becker, B. Pingault, H. Sternschulte, D. Steinmüller-Nethl, A. Gali, J. R. Maze, M. Atatüre, and C. Becher, Phys. Rev. Lett. **112**, 036405 (2014).

[10] J. N. Becker and E. Neu, in *Diamond for Quantum Applications Part 1*, Semiconductors and Semimetals, Vol. 103, edited by C. E. Nebel, I. Aharonovich, N. Mizuochi, and M. Hatano (Elsevier, Cambridge, MA, US, 2020), pp. 201–235.

[11] B. L. Green, S. Mottishaw, B. G. Breeze, A. M. Edmonds, U. F. S. D'Haenens-Johansson, M. W. Doherty, S. D. Williams, D. J. Twitchen, and M. E. Newton, Phys. Rev. Lett. **119**, 096402 (2017).

[12] M. H. Metsch, K. Senkalla, B. Tratzmiller, J. Scheuer, M. Kern, J. Achard, A. Tallaire, M. B. Plenio, P. Siyushev, and F. Jelezko, Phys. Rev. Lett. **122**, 190503 (2019).

[13] M. Zhong, M. P. Hedges, R. L. Ahlefeldt, J. G. Bartholomew, S. E. Beavan, S. M. Wittig, J. J. Longdell, and M. J. Sellars, Nature (London) **517**, 177 (2015).

[14] T. Utikal, E. Eichhammer, L. Petersen, A. Renn, S. Gtzinger, and V. Sandoghdar, Nat. Commun. **5**, 3627 (2014).

[15] P. Siyushev, K. Xia, R. Reuter, M. Jamali, N. Zhao, N. Yang, C. Duan, N. Kukharchyk, A. D. Wieck, R. Kolesov, and J. Wrachtrup, Nat. Commun. **5**, 3895 (2014).

[16] T. A. Abtew, W. Gao, X. Gao, Y. Y. Sun, S. B. Zhang, and P. Zhang, Phys. Rev. Lett. **113**, 136401 (2014).

[17] H. Seo, M. Govoni, and G. Galli, Sci. Rep. **6**, 20803 (2016).

[18] H. Seo, H. Ma, M. Govoni, and G. Galli, Phys. Rev. Materials **1**, 075002 (2017).

[19] P. J. Wellmann, Semicond. Sci. Technol. **33**, 103001 (2018).

[20] J. Davidsson, V. Ivády, R. Armiento, N. T. Son, A. Gali, and I. A. Abrikosov, New J. Phys. **20**, 023035 (2018).

[21] J.-I. Iwata, C. Shinei, and A. Oshiyama, Phys. Rev. B **93**, 125202 (2016).

[22] J. Davidsson, V. Ivády, R. Armiento, T. Ohshima, N. T. Son, A. Gali, and I. A. Abrikosov, Appl. Phys. Lett. **114**, 112107 (2019).

[23] P. A. Schultz, R. M. Van Ginhoven, and A. H. Edwards, Phys. Rev. B **103**, 195202 (2021).

[24] H. Ma, M. Govoni, and G. Galli, npj Comput. Mater. **6**, 85 (2020).

[25] M. Bockstedte, F. Schütz, T. Garratt, V. Ivády, and A. Gali, npj Quantum Mater. **3**, 31 (2018).

[26] Y. Wang, Q. Lin, and P. X.-L. Feng, Opt. Express **29**, 1011 (2021).

[27] I. Chatzopoulos, F. Martini, R. Cernansky, and A. Politi, ACS Photonics **6**, 1826 (2019).

[28] S. Castelletto, M. Barbiero, M. Charnley, A. Boretti, and M. Gu, Phys. Rev. Applied **14**, 034021 (2020).

[29] S. Choi, M. Jain, and S. G. Louie, Phys. Rev. B **86**, 041202 (2012).

[30] Y. Ma, M. Rohlfing, and A. Gali, Phys. Rev. B **81**, 041204 (2010).

[31] M. Gerosa, F. Gygi, M. Govoni, and G. Galli, Nat. Mater. **17**, 1122 (2018).

[32] M. Del Ben, F. H. da Jornada, A. Canning, N. Wichmann, K. Raman, R. Sasanka, C. Yang, S. G. Louie, and J. Deslippe, Comput. Phys. Commun. **235**, 187 (2019).

[33] M. S. Hybertsen and S. G. Louie, Phys. Rev. B **34**, 5390 (1986).

[34] M. Rohlfing and S. G. Louie, Phys. Rev. B **62**, 4927 (2000).

[35] B.-C. Shih, Y. Xue, P. Zhang, M. L. Cohen, and S. G. Louie, Phys. Rev. Lett. **105**, 146401 (2010).

[36] W. Gao, W. Xia, Y. Wu, W. Ren, X. Gao, and P. Zhang, Phys. Rev. B **98**, 045108 (2018).

[37] C. Friedrich, M. C. Müller, and S. Blügel, Phys. Rev. B **83**, 081101 (2011).

[38] Z. Ergönenc, B. Kim, P. Liu, G. Kresse, and C. Franchini, Phys. Rev. Materials **2**, 024601 (2018).

[39] D. Golze, M. Dvorak, and P. Rinke, Frontiers in Chemistry **7**, 377 (2019).

[40] S. G. Louie, Y.-H. Chan, F. H. da Jornada, Z. Li, and D. Y. Qiu, Nat. Mater. **20**, 728 (2021).

[41] L. Gordon, A. Janotti, and C. G. Van de Walle, Phys. Rev. B **92**, 045208 (2015).

[42] L. Torpo, T. E. M. Staab, and R. M. Nieminen, Phys. Rev. B **65**, 085202 (2002).

[43] T. Kobayashi, K. Harada, Y. Kumagai, F. Oba, and Y.-i. Matsushita, J. Appl. Phys. **125**, 125701 (2019).

[44] N. T. Son, P. Carlsson, J. ul Hassan, E. Janzén, T. Umeda, J. Isoya, A. Gali, M. Bockstedte, N. Morishita, T. Ohshima, and H. Itoh, Phys. Rev. Lett. **96**, 055501 (2006).

[45] M. Del Ben, F. H. da Jornada, G. Antonius, T. Rangel, S. G. Louie, J. Deslippe, and A. Canning, Phys. Rev. B **99**, 125128 (2019).

[46] J. P. Perdew, K. Burke, and M. Ernzerhof, Phys. Rev. Lett. **77**, 3865 (1996).

[47] J. R. Chelikowsky, N. Troullier, and Y. Saad, Phys. Rev. Lett. **72**, 1240 (1994); L. Kronik, A. Makmal, M. L. Tiago, M. M. G. Alemany, M. Jain, X. Huang, Y. Saad, and J. R. Chelikowsky, Phys. Status Solidi B **243**, 1063 (2006).

[48] Y. Zhou, Y. Saad, M. L. Tiago, and J. R. Chelikowsky, Phys. Rev. E **74**, 066704 (2006); K.-H. Liou, C. Yang, and J. R. Chelikowsky, Comp. Phys. Commun. **254**, 107330 (2020); K.-H. Liou, A. Biller, L. Kronik, and J. R. Chelikowsky, J. Chem. Theory and Comp. **17**, 4039 (2021).

[49] Z. Li and R. C. Bradt, J. Mater. Sci. **21**, 4366 (1986).

[50] J. Deslippe, G. Samsonidze, D. A. Strubbe, M. Jain, M. L. Cohen, and S. G. Louie, Comput. Phys. Commun. **183**, 1269 (2012).

[51] D. R. Hamann, Phys. Rev. B **88**, 085117 (2013).

[52] M. Schlipf and F. Gygi, Comput. Phys. Commun. **196**, 36 (2015).

[53] P. Scherpelz, M. Govoni, I. Hamada, and G. Galli, J. Chem. Theory Comput. **12**, 3523 (2016).

[54] P. Giannozzi, O. Andreussi, T. Brumme, O. Bunau, M. B. Nardelli, M. Calandra, R. Car, C. Cavazzoni, D. Ceresoli, M. Cococcioni, N. Colonna, I. Carnimeo, A. D. Corso, S. de Gironcoli, P. Delugas, R. A. D. Jr, A. Ferretti, A. Floris, G. Fratesi, G. Fugallo *et al.*, J. Phys.: Condens. Matter **29**, 465901 (2017).

[55] P. Giannozzi, S. Baroni, N. Bonini, M. Calandra, R. Car, C. Cavazzoni, D. Ceresoli, G. L. Chiarotti, M. Cococcioni, I. Dabo, A. Dal Corso, S. de Gironcoli, S. Fabris, G. Fratesi, R. Gebauer, U. Gerstmann, C. Gougoussis, A. Kokalj, M. Lazzeri,

L. Martin-Samos *et al.*, J. Phys.: Condens. Matter **21**, 395502 (2009).

[56] R. W. Godby, M. Schlüter, and L. J. Sham, Phys. Rev. B **37**, 10159 (1988).

[57] S. Lebègue, B. Arnaud, M. Alouani, and P. E. Bloechl, Phys. Rev. B **67**, 155208 (2003).

[58] M. Govoni and G. Galli, J. Chem. Theory Comput. **11**, 2680 (2015).

[59] T. A. Pham, H.-V. Nguyen, D. Rocca, and G. Galli, Phys. Rev. B **87**, 155148 (2013).

[60] H.-V. Nguyen, T. A. Pham, D. Rocca, and G. Galli, Phys. Rev. B **85**, 081101 (2012).

[61] L. Hung, F. H. da Jornada, J. Souto-Casares, J. R. Chelikowsky, S. G. Louie, and S. Öüt, Phys. Rev. B **94**, 085125 (2016).

[62] W. Gao, W. Xia, X. Gao, and P. Zhang, Sci. Rep. **6**, 36849 (2016).

[63] Appendix c: Major physical properties of common sic polytypes, in *Fundamentals of Silicon Carbide Technology* (John Wiley & Sons, Ltd, Singapore, 2014), pp. 521–524.

[64] K. Momma and F. Izumi, J. Appl. Crystallogr. **44**, 1272 (2011).

[65] J. R. Maze, A. Gali, E. Togan, Y. Chu, A. Trifonov, E. Kaxiras, and M. D. Lukin, New J. Phys. **13**, 025025 (2011).

[66] W. Gao and J. R. Chelikowsky, J. Chem. Theory Comput. **15**, 5299 (2019).

[67] T. Sommerfeld, J. Chem. Theory Comput. **9**, 4866 (2013).

[68] V. Ivády, I. A. Abrikosov, and A. Gali, npj Comput. Mater. **4**, 76 (2018).